OPTIMIZATION OF TOOTH-ROOT PROFILE FOR MAXIMUM LOAD-CARRYING CAPACITY: SPUR AND BEVEL GEARS

Mathew Shaker, Ting Zou, Jorge Angeles, Alexei Morozov
Centre for Intelligent Machines & Department of Mechanical Engineering, McGill University, Montreal, QC, Canada
Email: mathew.shaker@mail.mcgill.ca; ting@cim.mcgill.ca; angeles@cim.mcgill.ca; alexvit@cim.mcgill.ca

ABSTRACT

Increasing the strength of gears is a recurrent demand from industry. The authors report a novel approach to the design of tooth-root profile of spur and bevel gears, with the aim of reducing stress concentration, thereby increasing the gear-tooth load-carrying capacity. Bevel gears generated using the Tredgold approximation are considered. An iterative co-simulation consisting of tooth-root profile shape synthesis via nonlinear programming and finite element software tools is conducted, with the purpose of forming the tooth-root geometry with the minimum stress concentration. The proposed designs are capable of reducing the stress concentration by 21.0% in spur gears and 15.9% in bevel gears, over their conventional circular-filleted counterparts. Hence, the results showcase an innovative and sound methodology for the design of the tooth-root profile to increase gear load-carrying capacity.

Keywords: spur gear; bevel gear; tooth root bending stress; cubic splines; finite element analysis.

OPTIMISATION DE LA RACINE DES PROFILS DE DENTS POUR LA RÉSISTANCE MAXIMALE: DES ENGRENAGES PLANAIRES ET CONIQUES

RÉSUMÉ

Augmenter la résistance des dents d'engrenages est une éxigeance récurrente dans les industries. Les auteurs proposent une nouvelle approche à la conception de la racine des profils de dents des engrenages planaires et coniques, afin d'augmenter la résistance des engrenages. Des engrenages coniques générés en utilisant l'approximation de Tredgold ont été étudiés. Une procédure itérative de co-simulation consistant en la synthèse de la racine des profils de dents, par programmation non-linéaire et analyse par éléments finis, fut mise en place, afin de diminuer la concentration des contraintes à la racine des profils de dents. Les profils ainsi proposées permirent de réduire la concentration des contraintes de 21.0% pour les engrenages planaires et 15.9% pour les engrenages coniques. Donc, les resultats presentent une nouvelle méthodologie pour la conception de la racine des profils de dents des engrenages, ayant le but d'augmenter la résistance de ces derniers.

Mots-clés : engrenages planaires ; engrenages coniques ; résistance d'engrenages ; spline cubiques ; analyse par éléments finis.

1. INTRODUCTION

A growing demand for gears with higher load-carrying capacity and increased fatigue life accompanies the fast development of automotive transmissions. In order to achieve this goal, several avenues can be explored: novel materials; novel manufacturing techniques; or novel gear-tooth geometries [1]. As the key component in gear transmission systems, the stability and reliability of the gears play a significant role in the performance of the gear transmission system. Under working conditions, the gear tooth is exposed to

a combination of several effects, such as stress concentration, misalignment, tooth error, etc. [2]. When transmitting loads, each gear tooth behaves as a cantilever beam, subjected to bending. The maximum bending stress of the gear tooth evolves from the accumulation of normal stress under bending and appears at the root fillet. The gear tooth root is exposed to a combination of both shearing and bending [3]. The stress intensity factor and working life of a gear tooth is highly dependent on the tooth-root stress [4]. The first initial crack at the gear tooth often appears at regions that are affected the most by root stress concentration. Moreover, fatigue failure of tooth-root is also caused by the stress at the tooth root [1]. Within the development history of gear design, gear tooth fatigue due to bending is always a challenge to designers.

Precise verification of tooth strength calls for application of experimental technologies, such as electroresistive or piezoresistive. Though experimental testing is necessary for verifying numerical results, this is often expensive and complicated [5]. The Finite Element Method (FEM) is a computational tool most often used to calculate bending stress, strain and deformation [6]. Finite Element Analysis (FEA) provides a reliable tool to asses the response of physical systems even under nonlinear conditions [7].

The circular-filleted tooth root is widely used in the design of the gear tooth-roots [1, 8]. Due to a curvature discontinuity at the blending points of the circular fillet with the involute tooth profile and the root circle, stress concentration occurs at those points; such discontinuities cause a drastic jump in stress values, thereby leading to mechanical failure. Hence, the optimization of the gear tooth-root profile plays a significant role in reducing stress concentration, thereby improving gear-tooth strength.

In this paper, an innovative optimization procedure combining shape synthesis via nonlinear programming and FEA software tools is developed to produce the tooth-root fillet with the minimum stress concentration, in spur and bevel gears. The FEA results show a significant reduction in the maximum von Mises stress of the optimum tooth profiles when compared with their circular counterparts.

2. GEOMETRIC MODELLING OF THE GEAR TEETH

2.1. Spur Gears

Figure 1 illustrates the 2-D geometry of an involute spur gear tooth, with the dimensions listed in Table 1. The parameter values of the spur gear used in this simulation work are those reported by Ristić [5]. The gear tooth is built using the coordinate frame *Oxy* with origin at the center of the gear, its *y*-axis being the axis of symmetry of the gear tooth.

Table 1. Dimensions of the spur gear model

number of teeth N	20
module m (mm)	24
face width (mm)	50
pressure angle α_C $(^\circ)$	20
addendum circle radius r_a (mm)	264
pitch circle radius r_p (mm)	240
base circle radius r_b (mm)	225.526
dedendum circle radius r_d (mm)	210

The involute profile has found widespread applications in gear tooth design, due to its ease of high-precision manufacturing, low transmission error, silent operation as well as simplicity of assembly, arising from its robustness to errors in the distance between gear axes [9, 10]. The involute $\overset{\frown}{AB}$, shown in Fig. 1 is

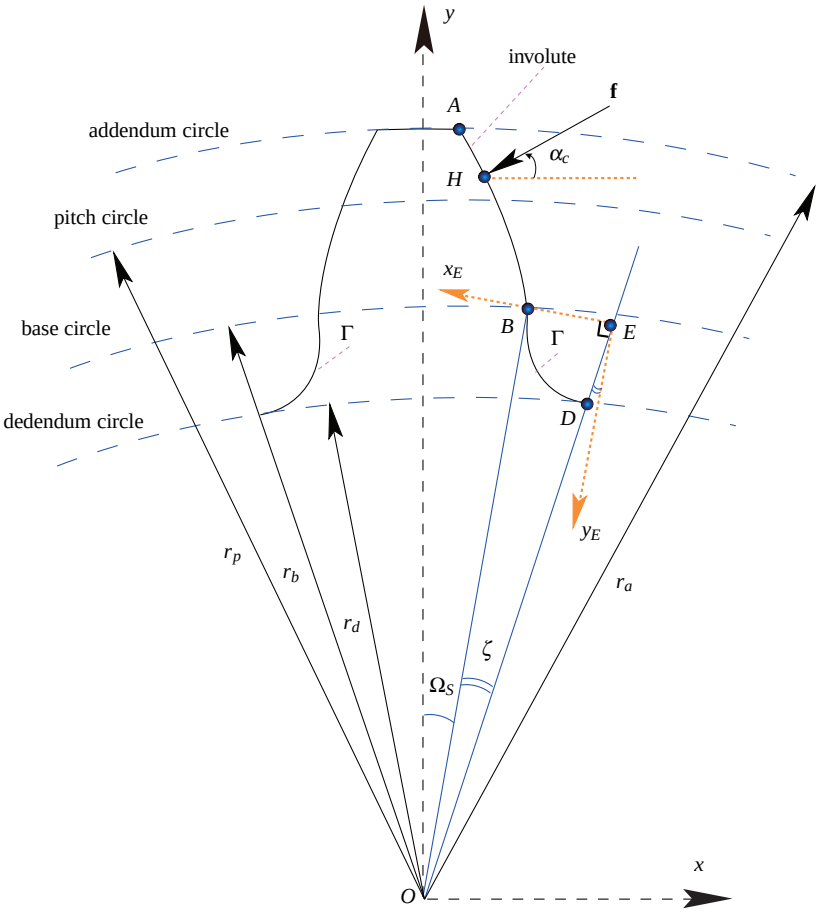

Fig. 1. Geometry of the spur gear tooth

defined by

$$\begin{cases} x_{inv} = r_b(\cos t + t\sin t) \\ y_{inv} = r_b(\sin t - t\cos t) \end{cases}, \quad 0 \le t \le \sqrt{\frac{r_a^2}{r_b^2} - 1} \tag{1}$$

The curve segment Γ, which blends the involute at point B and the dedendum circle at point D, functions as the gear tooth-root fillet. Γ is commonly produced in gear design as a circular arc connection [5, 11]. However, the problem with the circular root fillet lies in that it provides only first order geometric continuity, G^1, that is, position and tangent-continuity, which gives rise to stress concentration due to curvature discontinuities at the blending points [12]. Further, the local stress concentration caused by geometrical discontinuities may lead to mechanical failure [13]. In order to reduce the stress concentration, an important criterion, G^2-continuity at the blending of two given curve segments, should be satisfied. G^2-continuity means position, tangent and curvature continuity over a given geometric curve [14]. Hence, the problem at hand is formulated as the optimization of the root profile, as implemented by an optimum curve connecting the blending points B and D with G^2-continuity *as smoothly as possible*.

Further, to investigate the bending strength of the gear tooth, a normal force **f**, the full load transmitted, as shown in Fig. 1, is considered to be exerted at the highest point of single tooth contact (HPSTC) of the gear—Point H in the same figure.

2.2. Bevel Gears

A *virtual spur gear*, as illustrated in Fig. 2, is generated via the projection of a Tredgold approximation (TA) bevel gear onto the Tredgold plane [15–17]. The Tredgold plane, by definition, is tangent to the back cone of a bevel gear, or in other words, it rolls on the surface of the back cone [18]. Therefore, for a bevel gear set, the Tredgold plane for each gear rolls on the surface of the corresponding back cone.

The virtual spur gear has a pitch radius r_b equal to the back cone distance and same pitch as the bevel gear [19]. The number of teeth N' of the virtual spur gear is given by

$$N' = \frac{2\pi r_b}{p} \tag{2}$$

where p is the circular pitch measured at the heel. In this light, N' is not necessarily an integer.

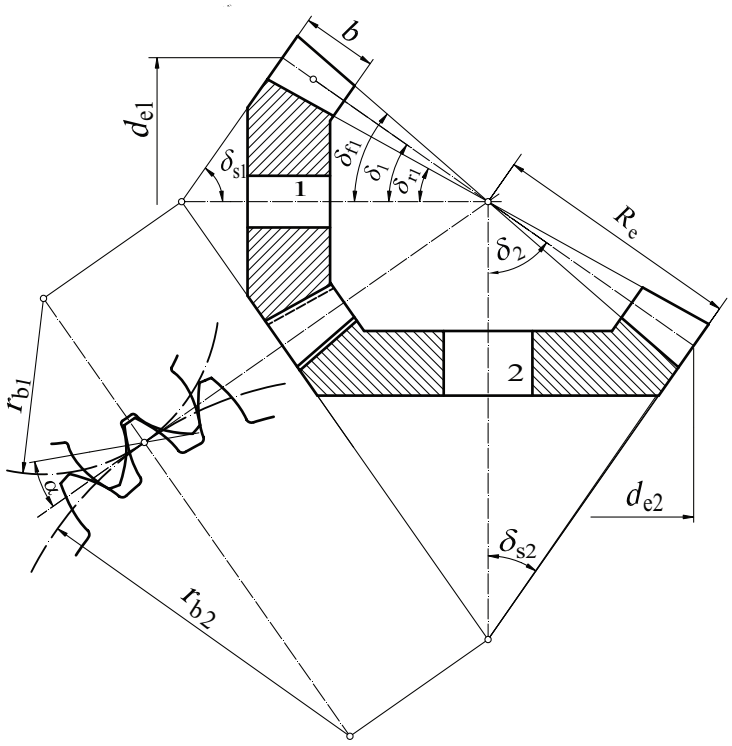

Fig. 2. Straight bevel gear parameters

A bevel pinion belonging to a differential gear set manufactured by Linamar Corporation, an industrial partner of the Automotive Partnership Canada project at McGill University, is used in this research. The parameters of the bevel pinion are given in Table 2.

3. METHODOLOGY

3.1. Curve Synthesis

For the purpose of simplifying the curve-synthesis procedure, we resort to non-parametric cubic splines to discretize the tooth-root fillet [20]. Figure 3 includes a sketch of the blending segments—the involute and part of the dedendum circle—by means of a third one, Γ. The coordinate frame Ex_Ey_E is built with the y_E-axis parallell to $\overline{OB}$, as shown in Fig. 1. Notice that the segments in this figure pertain to a tooth in the lower half of the gear, as opposed to the tooth of Fig. 1, for ease of representation.

Table 2. Dimensions of bevel pinion

number of teeth N_1	9
mating gear teeth N_2	14
module m (mm)	5.7658
pressure angle α_c (°)	24
pitch angle δ (°)	32.735
face angle δ_f (°)	39.588
root angle δ_r (°)	24.530
face width b (mm)	22.5
virtual gear number of teeth N'	11

Further, $n+2$ points $\{P_k\}_0^{n+1}$ are defined along the mid-curve segment Γ, by their polar coordinates $P_k(\rho_k,\theta_k)$, with $P_0(\rho_0,\theta_0)=B$ and $P_{n+1}(\rho_{n+1},\theta_{n+1})=D$. For point P_k, let $\theta_k=\theta_0+k\Delta\theta$, for $k=1,2,\cdots,n+1$, the uniform increment $\Delta\theta$ being

$$\Delta\theta=\frac{\theta_{k+1}-\theta_0}{k+1} \tag{3}$$

Hence, the polar coordinates $\{\rho_k\}_1^{n+2}$ are assembled into one $(n+2)$-dimensional array as

$$\rho=[\rho_0,\rho_1,\cdots,\rho_{n+1}]^T \tag{4}$$

By the same token, the arrays of first- and second-order derivatives with respect to the polar coordinate θ of Fig 3, ρ' and ρ'', respectively, are defined likewise.

According to the definition of non-parametric cubic splines, the cubic polynomial $\rho_k(\theta)$ between two consecutive supporting points P_k and P_{k+1} takes the form [21]

$$\rho_k(\theta)=A_k(\theta-\theta_k)^3+B_k(\theta-\theta_k)^2+C_k(\theta-\theta_k)+D_k \tag{5}$$

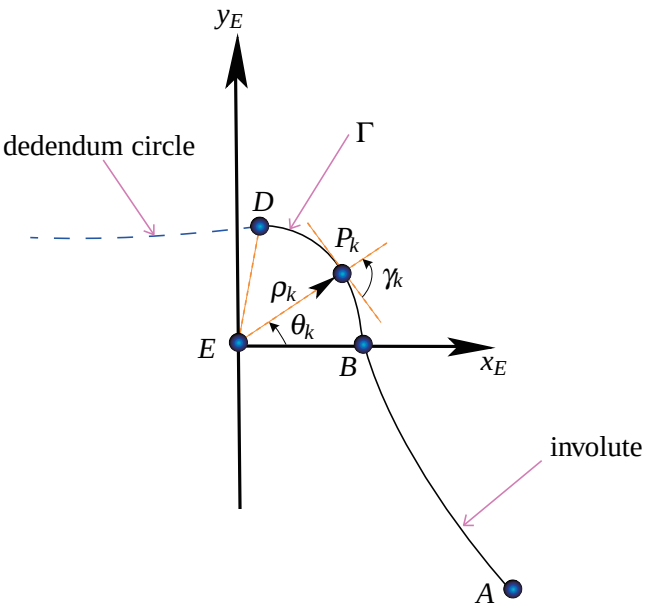

Fig. 3. The blending of the involute and root circle segment using a G^2-continuous curve fillet

in which $\theta_k \leq \theta \leq \theta_{k+1}$ and $0 \leq k \leq n$.

By virtue of the G^2-continuity condition, i.e., two curvatures coinciding at the kth blending point, $\rho_{\mathbf{k}}$, $\rho_{\mathbf{k}}{}'$ and $\rho_{\mathbf{k}}{}''$ and their counterparts at their neighbouring segments, are found to satisfy the linear relationships below [21]:

$$\mathbf{A}\rho'' = 6\mathbf{C}\rho, \quad \mathbf{P}\rho' = \mathbf{Q}\rho \tag{6}$$

with matrices **A**, **C**, **P** and **Q** provided in the Appendix.

Further, the curvature at P_k takes the form

$$\kappa_k = \frac{\rho_k^2 + 2(\rho_k')^2 - \rho_k\rho_k''}{[\rho_k^2 + (\rho_k')^2]^{3/2}} \tag{7}$$

Now, if a curve with "the smallest possible curvature is sought", an obvious candidate is a curve Γ with a curvature distribution that carries the minimum root-mean-square value of its curvature in the segment comprised between B and D of Fig. 1. Hence, the optimization problem is formulated as

$$\begin{aligned} &z = \frac{1}{n}\sum_{k=1}^{n} w_k\kappa_k^2 \longrightarrow \min_{\mathbf{x}}, \quad \mathbf{x} = [\rho_1 \quad \cdots \quad \rho_n]^T \\ &\text{subject to} \\ &\kappa_0(\rho,\rho',\rho'') = \kappa_B = 0, \quad \kappa_{n+1}(\rho,\rho',\rho'') = \kappa_D = \frac{1}{r_d} \end{aligned} \tag{8}$$

in which $w_k > 0$ denotes the normal weight at point P_k, obeying $\sum_{k=1}^{n} w_k = 1$. Besides, with reference to Fig. 1, the additional boundary constraints at the two blending points are

$$\begin{cases} \theta_0 = \theta_B = 0 \\ \theta_{n+1} = \theta_D = \dfrac{\pi}{2} - \zeta_m \end{cases}, \quad \begin{cases} \rho_0 = \rho_B = r_b \tan\zeta_m \\ \rho_{n+1} = \rho_D = \dfrac{r_b}{\cos\zeta_m} - r_d \end{cases} \tag{9}$$

The optimization problem thus formulated is a constrained nonlinear program, which can be solved using a suite of methods, the one used here is the in-house developed ODA (orthogonal decomposition algorithm) [22].

The foregoing curve synthesis procedure is used for spur- and bevel-gear tooth-root profile optimization. While its implementation is obvious in the spur gear case, in bevel gears it depends on the method of generation. In this research work the TA method is considered for bevel-gear generation.

3.2. Co-simulation

Upon the geometry synthesis of the root profile, the optimization problem formulated in Sec. 3.1 is implemented via a co-simulation among: the ODA package, implemented in Matlab; modelling, using SolidWorks Application Programming Interface (API); and FEA, using a customized ANSYS Parametric Design Language (APDL). Figure 4 illustrates the flowchart of the gear tooth-root profile optimization procedure. In the spur gear case, both modelling and FEA were done on ANSYS using APDL. However, bevel-gear modelling, which requires more advanced solid modelling techniques, was implemented using a customized macro in VisualBasic.NET format on SolidWorks. The software packages were coupled together to interact in an automated iterative procedure to solve the structural optimization problem.

The procedure starts with equal weights for all supporting points, i.e., $w_k = 1/n$, the coordinates for all supporting points being generated to form the initial cubic-splined tooth profile. The optimum found with equal weights is termed the *geometric optimum*. Based on the G^2-continuity constraints, the geometric

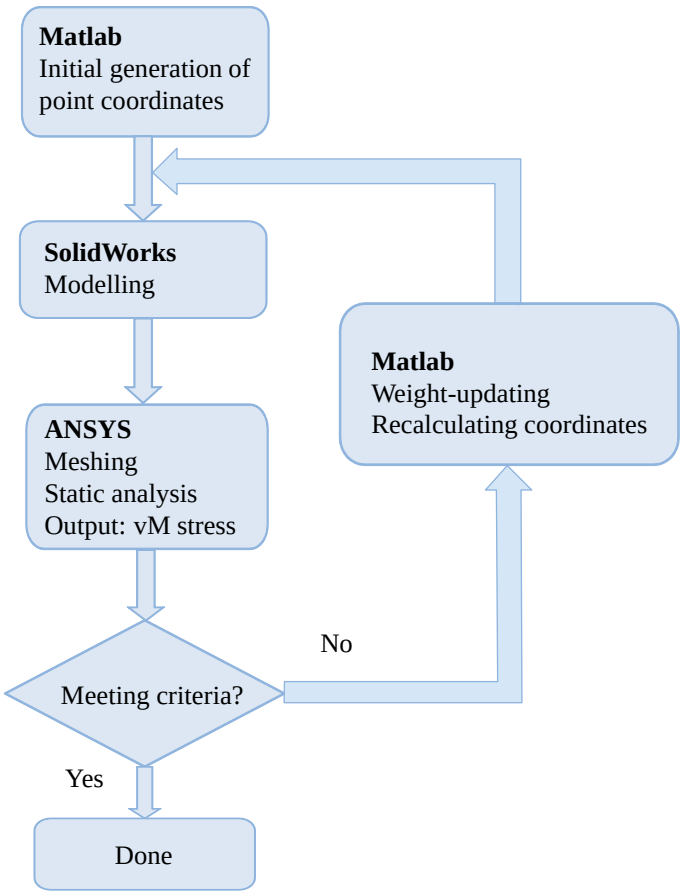

Fig. 4. Root curve optimization flowchart

optimum is capable of reducing the stress concentration to some extent. However, there is still room for improvement. Hence, a set of iterations is conducted, to find the root profile with minimum von Mises stress distribution.

The supporting-point coordinates of the geometrically optimum fillet obtained from Matlab are used to model the gear tooth. Then, a static analysis is conducted by applying the boundary conditions and loadings, which produces the von Mises stress for each supporting point along the root-fillet profile. Aiming to alleviate the stress concentration along the splined fillet, different weights in eq. (8) are assigned to each supporting point according to their corresponding von Mises stress values s_k, as reported by ANSYS:

$$w_k = \frac{s_k}{\sum_{i=1}^{n} s_i} \tag{10}$$

The idea is that curvature values are penalized by means of weights proportional to their von Mises stress values. The problem previously formulated is solved again but with non-uniform weight coefficients, until the von Mises stress distribution becomes fairly uniform. The process helps approach Venkayya's criterion [1] of achieving an almost uniform stress distribution at the critical region of the optimum fillet [23]. This fillet is termed the *structural optimum*.

[1] According to Venkayya's criterion, the optimum design refers to the one in which the strain energy per unit volume stays constant.

4. SIMULATION RESULTS

4.1. FE Model Formulation

As shown in Fig. 5a, quadratic 4-node PLANE182 elements were used on ANSYS 14.0 to discretize the spur-gear tooth domain. The mesh is refined at the gear tooth fillet, for the purpose of accurate prediction of the stress concentration at the fillet. The boundary conditions on the generated FE model are defined by displacement constraints over the inner rim and the other two border surfaces, which separate the modeled gear tooth from the rest of the gear body. Besides, a $1000(\cos 20^\circ)$ N tangential load that the gear transmits is applied as an external force on the FE model, at its HPSTC, averagely distributed along the contact line over the tooth width.

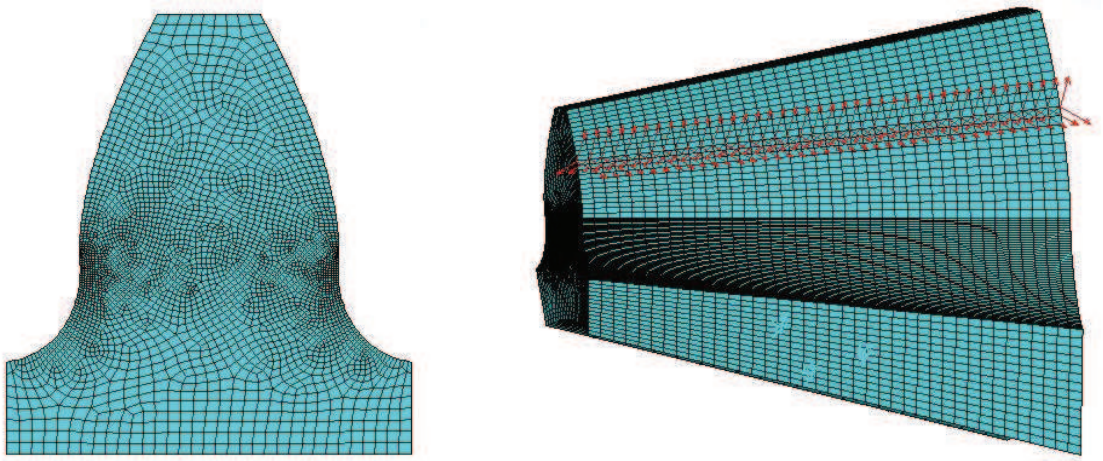

(a) Spur gear tooth (b) Bevel gear tooth

Fig. 5. Finite Element Mesh

The bevel gear tooth model was generated on SolidWorks 2013 and then imported into ANSYS for static analysis. To model the TA bevel gear, the virtual spur gear on the Tredgold plane is used to create the tooth cut, as shown in Fig. 6. A 2D sketch of the tooth space of the virtual spur gear is created on the Tredgold plane and tapered smoothly towards the apex and used to cut the gear. Through rotation copying the tooth spaces, the full gear geometry was accomplished.

The bevel gear tooth is meshed using 8-node brick SOLID185 elements which are suitable for the 3D modelling of solid structures. The sweep-mesh approach is used to sweep the mesh from the tooth heel through the volume (to the toe). The FE model for the TA bevel gear tooth is shown in Fig. 5b. The displacements over the inner tooth hub and the cut boundaries of the bevel gear tooth were constrained. A $1000(\cos 20^\circ)$ N tangential load is applied as an external force on the FE model, at its HLSTC.

The material used in the simulations is structural steel, with a Young modulus of 2.1×10^{11} Pa, a Poisson ratio of 0.3, and a density of 7870 $\mathrm{kg/m^3}$.

4.2. FEA Results

A set of iterations was conducted to reach the optimum shape profile of the spur and bevel-gear tooth-root, as described in this section.

The optimization procedure stopped at its seventh iteration in the spur gear case, when the maximum stress reduced from the previous iteration is smaller than 0.01 MPa. The maximum von Mises stress versus the number of iterations is illustrated in Fig. 7, from which we can observe that the maximum von Mises

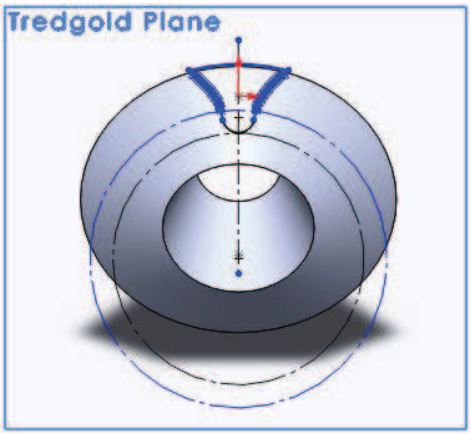

(a) Tredgold Plane

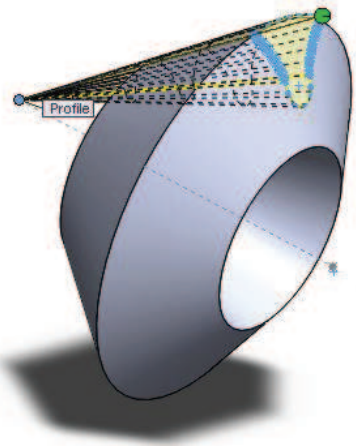

(b) Lofted cut

Fig. 6. TA bevel gear CAD modelling

stress value shows a significant decrement at the first and second iterations; then, it starts settling down to the minimum.

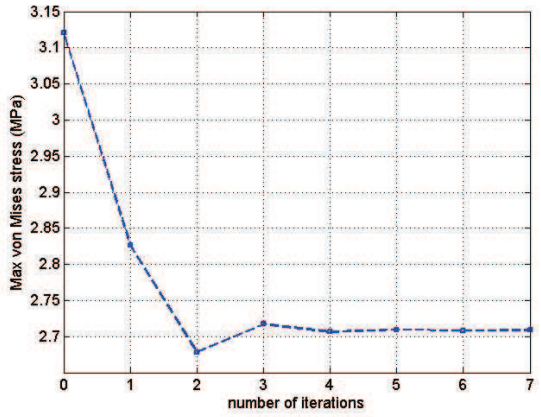

Fig. 7. Maximum vM stress vs. number of iterations

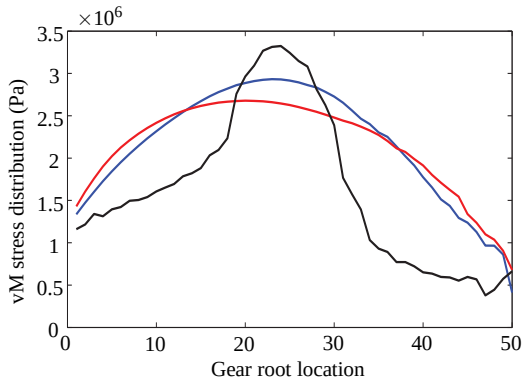

Fig. 8. vM stress distribution on circular (black), geometrically optimum (blue) and structurally optimum (red) fillets

The von Mises stress distributions of the two optimum fillets are plotted in Fig. 9. The maximum von Mises stress values σ_{vm} for different root curve shapes are compared and listed in Table 3. It is apparent that, compared to its circular counterpart, the geometric optimum is capable of reducing the σ_{vm} by 15.1%. The structural optimum shows a better performance in the reduction of σ_{vm}, of around 21% over the conventional circular fillet.

In addition, the von Mises stress distributions of the three above-mentioned fillet types are plotted in Fig. 8, in which the abscissa denotes the node number along the gear tooth-root profile. It is observed that the structurally optimum fillet not only reduces the maximum von Mises stress, but also smoothes the stress distribution along the whole root profile, thereby meeting the design objectives.

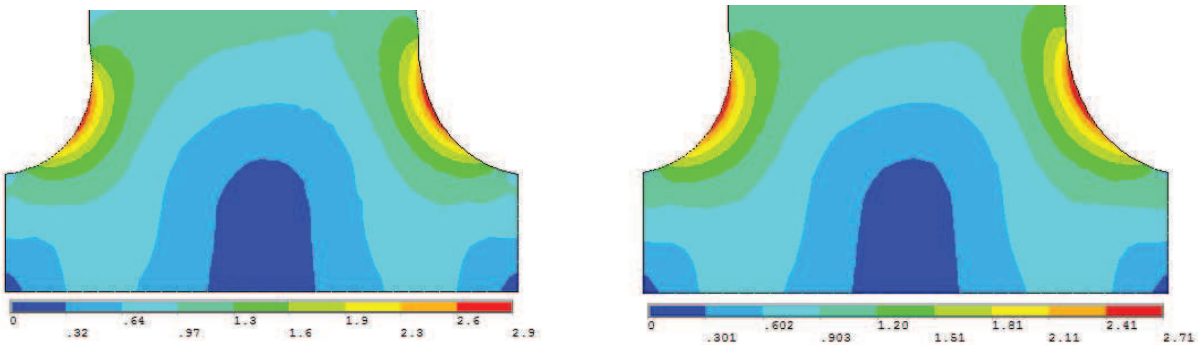

(a) Geometrically optimum

(b) Structurally optimum

Fig. 9. vM stress distribution plots of the spur gear

Table 3. Maximum von Mises stress in different spur gear tooth-root curve types

root curve type	von Mises σ_{vm} (MPa)
Circular	3.301
Cubic spline (geometrically optimum)	2.802
Cubic spline (structurally optimum)	2.6084

In the bevel gear case the optimization procedure stopped at the sixth iteration. A similar behaviour is observed here: starting from an initial guess, the maximum von Mises stress drops significantly in the first and second iterations, and then starts settling down to the minimum, as shown in Fig. 10.

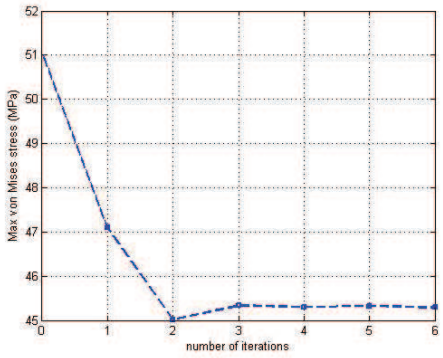

Fig. 10. Maximum vM Stress vs. number of iterations

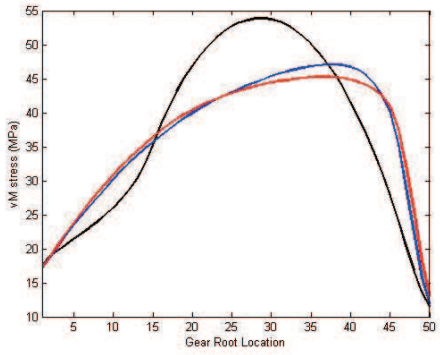

Fig. 11. vM stress distribution on circular (black), geometrically optimum (blue) and structurally optimum (red) fillets

The von Mises stress distributions of the optimum fillets are shown in Fig. 12, and the maximum von Mises stress values are given in Table 4. The von Mises reduction rate is 12.6% in the geometrically optimum fillet and 15.9% in its structurally optimum counterpart, compared with the circular-filleted tooth-root.

5. CONCLUSIONS

The tooth-root profile optimization for spur and bevel gears, designed for maximum load-carrying capacity, is reported in this paper. Under working bending load, the maximum von Mises stress of the proposed

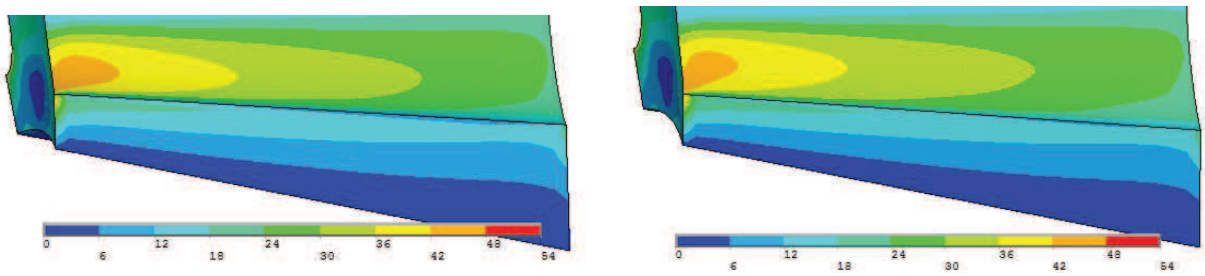

(a) Geometrically optimum

(b) Structurally optimum

Fig. 12. von Mises stress distributions for bevel gear

Table 4. Maximum von Mises stress in different bevel gear tooth-root curve types

root curve type	von Mises σ_{vm} (MPa)
Circular	53.88
Cubic spline (geometrically optimum)	47.093
Cubic spline (structurally optimum)	45.294

spline-filleted root profiles were analyzed and compared with their circular-filleted counterparts. Both the geometric and the structural optima are analyzed. The maximum von Mises stress reduction in the structural optima was 15.1% and 21% in spur and bevel gears respectively, of the corresponding circular-filleted counterpart profile. Moreover, the stress distributions along the gear tooth-root profiles was also studied, by recording the maximum von Mises stress value at each node of the FE model on the root profile. The stress distribution of the structural optimum root profiles were the smoothest. The stress concentration of the proposed root profiles were significantly reduced.

ACKNOWLEDGEMENTS

The support from Canada's NSERC through the Automotive Partnership Canada project, grant number APCPJ418901-11, is highly acknowledged.

REFERENCES

1. Spitas, V., Costopoulos, T., and Spitas, C., 2005. "Increasing the strength of standard involute geat teeth with novel circular root fillet design". *American Journal of Applied Sciences,* ***2***(6), pp. 1058–1064.
2. Tiwari, S. K., and Joshi, U. K., 2012. "Stress analysis of mating involute spur gear tooth". *International Journal of Engineering Research & Technology,* ***1***(9), pp. 1–11.
3. Kawalec, A., Wiktor, J., and Ceglarek, D., 2005. "Comparative analysis of tooth-root strength using iso and agma standard in spur and helical gear with FEM-based verification". *Journal of Mechanical Design, ASME,* ***128***(5), pp. 1141–1158.
4. Pedrero, J. I., Vallejo, I. I., and Pleguezuelos, M., 2006. "Calculation of tooth bending strength and surface durability of high transverse contact ratio spur and helical gear drives". *Journal of Mechanical Design, ASME,* ***129***(1), pp. 69–74.
5. Ristić, D., 2009. "Numerical model for the critical stress determination in spur gears". *Scientific Technical Review,* ***LVIX***(1), pp. 78–86.
6. Li, X., Jiang, S., Li, C., and Huang, B., 2013. "Statics analysis of cylindrical gear drive at any meshing position based on ansys". *Journal of Theoretical and Applied Information Technology,* ***47***(2), pp. 767–773.
7. Atanasovska, I., Nikolić-Stanojlović, V., Dimitrijević, D., and Momcilović, D., 2009. "Finite element model of

stress analysis and nonlinear contact analysis of helical gears". *Scientific Technical Review,* ***LVIX***(1), pp. 61–69.
8. Senthilvelan, S., and Gnanamoorthy, R., 2006. "Effect of gear tooth fillet radius on the performance of injection molded nylon 6/6 gears". *Materials and Design,* ***27***(8), pp. 632–639.
9. Litvin, F. L., and Fuentes, A., 2004. *Gear Geometry and Applied Theory*, Second ed. Cambridge University Press, Cambridge, UK.
10. Radzevich, S. P., 2012. *Dudley's Handbook of Practical Gear Design and Manufacture*, Second ed. CRC Press, Boca Raton, FL.
11. Sankar, S., Raj, M., and Nataraj, M., 2010. "Profile modification for increasing the tooth strength in spur gear using CAD". *Engineering,* ***2***(9), pp. 740–749.
12. Neuber, H., 1961. *Theory of Notch Stresses: Principles for Exact Calculation of Strength with Reference to Structural Form and Material*. United States Atomic Energy Commission, Office of Technical Information, Translation Series.
13. Collins, J. A., 1993. *Failure of Materials in Mechanical Design: Analysis, Prediction, Prevention*, Second ed. John Wiley & Sons, Inc., New York.
14. Angeles, J., 1983. "Synthesis of plane curves with prescribed geometric properties using periodic splines". *Computer-Aided Design,* ***15***(3), pp. 147–155.
15. Shigley, J., M. C., and Budynas, R., 2004. *Mechanical Engineering Design*, seventh ed. McGraw-Hill Companies, Inc.
16. Figliolini, G., Stachel, H., and Angeles, J., 2009. "The computational fundamentals of spatial cycloidal gearing". In Kecskeméthy, A., Müller, A. (eds): Computational Kinematics, Proc. of the 5th Internat. Workshop on Computational Kinematic, Dortmund, pp. 375–384.
17. Dooner, D. B., 2012. *Kinematic Geometry of Gearing*. John Wiley.
18. Radzevich, S. P., 2013. *Theory of Gearing: Kinematics, Geometry, and Synthesis*. CRC Press, Boca Raton, FL.
19. Elkholy, A. H., Elsharkawy, A. A., and Yigit, A. S., 1998. "Effect of meshing tooth stiffness and manufacturing error on the analysis of straight bevel gears". *Mechanics of Structs Mach.,* ***26***(1), pp. 41–61.
20. Teng, C. P., Bai, S., and Angeles, J., 2008. "Shape synthesis in mechanical design". *Acta Polytechnica,* ***47***(6), pp. 56–62.
21. Späth, H., 1995. *One Dimensional Spline Interpolation Algorithms*. A. K. Peters Ltd., Wellesley, MA.
22. Teng, C. P., and Angeles, J., 2001. "A sequential-quadratic-programming algorithm using orthogonal decomposition with gerschgorin stabilization". *J. Mech. Des.,* ***123***(4), pp. 501–509.
23. Venkayya, V. B., 1971. "Design of optimum structures". *J. Computers and Structures,* ***1***, pp. 263–309.

APPENDIX: MATRICES RELATED TO THE G^2-CONTINUITY CONDITIONS

$$\mathbf{A} = \Delta\theta \begin{bmatrix} 2 & 1 & 0 & 0 & \cdots & 0 & 0 \\ 1 & 4 & 1 & 0 & \cdots & 0 & 0 \\ 0 & 1 & 4 & 1 & \cdots & 0 & 0 \\ \vdots & \vdots & \ddots & \ddots & \ddots & \vdots & \vdots \\ 0 & 0 & \cdots & 1 & 4 & 1 & 0 \\ 0 & 0 & 0 & \cdots & 1 & 4 & 1 \\ 0 & 0 & 0 & \cdots & 0 & 1 & 2 \end{bmatrix}, \quad \mathbf{C} = \frac{1}{\Delta\theta} \begin{bmatrix} c_{11} & 1 & 0 & 0 & \cdots & 0 & 0 \\ 1 & -2 & 1 & 0 & \cdots & 0 & 0 \\ 0 & 1 & -2 & 1 & \cdots & 0 & 0 \\ \vdots & \vdots & \ddots & \ddots & \ddots & \vdots & \vdots \\ 0 & 0 & \cdots & 1 & -2 & 1 & 0 \\ 0 & 0 & 0 & \cdots & 1 & -2 & 1 \\ 0 & 0 & 0 & \cdots & 0 & 1 & c_{n''n''} \end{bmatrix} \tag{11}$$

in which $n'' = n+2$, $c_{11} = -1 - \Delta\theta/\tan(\gamma_0)$ and $c_{n''n''} = -1 - \Delta\theta/\tan(\gamma_{n+1})$.

$$\mathbf{P} = \Delta\theta \begin{bmatrix} \frac{1}{\Delta\theta} & 0 & 0 & 0 & \cdots & 0 & 0 \\ 1 & 4 & 1 & 0 & \cdots & 0 & 0 \\ 0 & 1 & 4 & 1 & \cdots & 0 & 0 \\ \vdots & \vdots & \ddots & \ddots & \ddots & \vdots & \vdots \\ 0 & 0 & \cdots & 1 & 4 & 1 & 0 \\ 0 & 0 & 0 & \cdots & 1 & 4 & 1 \\ 0 & 0 & 0 & \cdots & 0 & 0 & \frac{1}{\Delta\theta} \end{bmatrix}, \mathbf{Q} = \frac{1}{\Delta\theta} \begin{bmatrix} \frac{1}{\tan(\gamma_0)} & 0 & 0 & 0 & \cdots & 0 & 0 \\ -3 & 0 & 3 & 0 & \cdots & 0 & 0 \\ 0 & -3 & 0 & 3 & \cdots & 0 & 0 \\ \vdots & \vdots & \ddots & \ddots & \ddots & \vdots & \vdots \\ 0 & 0 & \cdots & -3 & 0 & 3 & 0 \\ 0 & 0 & 0 & \cdots & -3 & 0 & 3 \\ 0 & 0 & 0 & \cdots & 0 & 0 & \frac{1}{\tan(\gamma_{n+1})} \end{bmatrix} \tag{12}$$